A Fully Integrated CMOS Accelerometer Using Bondwire Inertial Sensing

Yu-Te Liao, *Student Member, IEEE*, William J. Biederman, *Student Member, IEEE*, and Brian P. Otis, *Senior Member, IEEE*

***Abstract*—This paper presents the design, implementation, and characterization of a fully integrated accelerometer using a bondwire inertial sensor. The accelerometer was implemented in a standard CMOS process without microelectromechanical processing. The system consists of a gold and aluminum bondwire inertial sensor and readout circuitry. Finite-element analysis was used to characterize the mechanical performance of the accelerometer and reinforce empirical data. The system includes a fully differential frequency modulation downconversion architecture and consumes 13.5 mW while achieving a gain of 10 kHz/g, a bandwidth of 700 Hz, and a resolution of 80 mg. The chip was fabricated in an 0.13-μm CMOS process with an area of 1.1 mm^2.**

***Index Terms*—Accelerometer, bondwires, sensors.**

I. Introduction

MICROELECTROMECHANICAL (MEMS) inertial sensor technology was first developed in the 1980s and has traditionally been used in guidance, navigation, and control applications [1]. Recently, accelerometers have been incorporated into many types of mass-produced commercial products, such as automobiles, pedometers, mobile phones, PDAs, and gaming consoles. These new applications necessitate sensors that offer low-cost and miniaturization rather than high precision. As the number of applications in new markets increases, there will be further demand for accelerometers that are small, robust, have a low production cost, and have the capability for high-volume manufacturing [2].

The physical transduction mechanisms underlying MEMS accelerometers include capacitive, piezoresistive, piezoelectric, optical, and tunneling [3]–[7]. These sensors provide stable and accurate acceleration detection. Their fabrication cost, however, is relatively high due to their complicated structures and large size. Bulk micromaching techniques [8] were developed to integrate MEMS devices with electronic circuitry on the same substrate. Although this technique is successful, the post processing and wafer-level assembly reduce the flexibility and constrain the size of the proof mass. Since the actual sensing element is fabricated in a nonstandard technology [9], [10], the cost reductions are not as significant as they would be in a standard IC process.

The ability to integrate an accelerometer into any IC would enable many important capabilities, including device orientation, shock detection/prediction, and motion detection. Our proposed Acceleroemter comprises: 1) a technique for using standard IC bonding wires as inertial sensors and 2) a low-power readout circuit architecture that can be designed in any IC process. In order to implement an accelerometer that is compatible with a completely standard IC technology, we investigated the mechanical and electrical properties of bondwires, which are widely used to electrically connect a silicon chip to its package [11]. Bondwires are typically 1–5 mm long, have a 1-mil diameter, are composed of gold or aluminum, and trace an approximately parabolic arc. As process nodes shrink, bondpad pitches reduce, causing the mutual inductance between wires to become an increasingly large contributor to the total wire inductance. Under acceleration, bondwires exhibit mechanical deflection that is especially prominent at the apex of the parabolic curve [12]. Changing a bondwire's geometry or material will result in a change in the magnitude of the wire's deflection for a given acceleration. By controlling the material and/or geometry of two adjacent bondwires, the relative distance between the two can be altered under acceleration, causing changes in the magnetic coupling. Thus, the resulting change in mutual inductance is proportional to the package acceleration.

This paper is organized as follows. Section II presents the proposed sensing scheme. Section III presents the corresponding bondwire models, which are verified with finite-element method (FEM) simulations. The noise analysis of the mechanical and electrical system is shown in Section IV. Section V describes the system and circuit implementation, followed by the experimental results in Section VI. Finally, conclusions are briefly outlined in Section VII.

II. Proposed Sensing Scheme

Fig. 1 shows the diagram of the proposed sensing scheme using a bondwire inertial sensor. A dense and relatively elastic gold (Au) wire is used in conjunction with a stiff and less dense aluminum (Al) wire. The difference in material properties creates a relative deflection between the two bondwires during acceleration. Table I shows the relevant mechanical properties of these two materials. Despite the fact that Au and Al have a similar Young's modulus, Au is 7.14 times denser than Al, resulting in a much greater bondwire displacement for the same applied

Manuscript received January 14, 2010; revised March 24, 2010; accepted May 20, 2010. Date of publication June 10, 2010; date of current version November 03, 2010. The associate editor coordinating the review of this manuscript and approving it for publication was Prof. Boris Stoeber.

Y.-T. Lao and B. P. Otis are with the Department of Electrical Engineering, University of Washington, Seattle, WA 98195-2500 USA (e-mail: yudo@u.washington.edu; botis@u.washington.edu).

W. Biederman is with the Department of Electrical and Computer Engineering, University of California, Berkeley, CA 94720 USA (e-mail: willbiederman@gmail.com).

Color versions of one or more of the figures in this paper are available online at http://ieeexplore.ieee.org.

Digital Object Identifier 10.1109/JSEN.2010.2052031

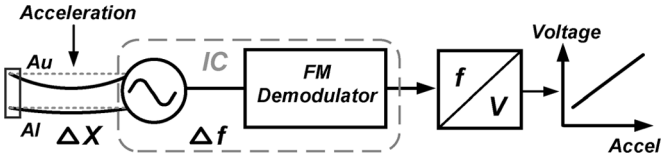

Fig. 1. Proposed sensing scheme.

TABLE I
BONDWIRE MATERIAL

Material	Au	Al
Young's modulus (GPa)	78	70
Density (g/cm^3)	19.3	2.7

acceleration. The peak displacement per acceleration of gravity (g) at the apex of a semicircular bondwire is derived as [12]

$$\frac{\Delta X}{g} = \frac{\rho R^4}{Er^2}(2\pi + \pi^2) \tag{1}$$

where R is the radius of the semicircle, r is the radius of the wire, E is the Young's modulus, and ρ is the density. Equation (1) demonstrates that the displacement is dependent on the configuration, radius and materials of bondwires. FEM simulation results of Au and Al wires in various configurations are presented in Section III. The relative displacement of adjacent bondwires creates mutual inductances changes which are converted to a frequency deviation by an oscillator. In the low-gigahertz range, bondwire inductors can have a quality factor between 30 and 70, improving the phase-noise performance of the low power front-end sensing circuitry. The oscillator has a large amplitude output (hundreds of millivolts), which is less sensitive to induced noise. The frequency-modulated signal offers immunity to amplitude noise and can be decoded and digitized by a conventional FM architecture. Section III presents analysis and simulation results describing the expected relative mechanical deflection from the bondwire sensor.

III. MECHANICAL AND ELECTRICAL MODELING OF THE INERTIAL SENSOR

A. Mechanical Modeling Using FEM Simulation

We used FEM techniques to find approximate solutions of integral and partial differential equations (PDE) to model the 3-D parabolic arc. A commercial FEM software package (*COMSOL Multiphysics*) was used to simulate the bondwire deflection under acceleration and characterize the performance of the sensor. The model of the bondwire sensor along with our coordinate reference is shown in Fig. 2. Intuitively, the structure is most compliant in the X-axis and much stiffer in the Y- and Z-axes. The performance metrics of an inertial sensor include mechanical sensitivity, bandwidth, linearity, isolation between axes, and resolution. The mechanical gain is a measure of displacement versus acceleration. Fig. 3 shows the simulated difference in the magnitude of deflection for bondwires with different length, diameter, and arc height. As the length and arc height increase, the amount of mass suspended by the clamped ends increases, causing a larger force to be applied to the wire under the same acceleration. However, the arc height is limited by the IC package and the ability of the wirebonder

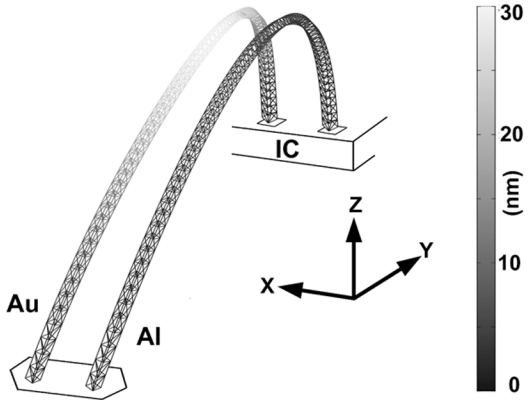

Fig. 2. FEM simulation of the bondwire deflection for 1-g acceleration along the X-axis.

to accurately reproduce bonds. Additionally, the smaller the bondwire diameter, the larger the displacement the bondwire will experience due to a decrease in stiffness. Fig. 4(a) shows the difference between Au and Al bondwire deflections along all three axes. The bondwires exhibit the largest relative displacement along the X-axis, which is 20 times larger than in the Y-axis and 100 times larger than in the Z-axis.

B. Resonant Frequency

In this open-loop inertial sensor system, the operational bandwidth is determined by the mechanical resonant frequency (ω_r) of the bondwires. At ω_r, the bondwire displacement is amplified by the mechanical quality factor (Q_{Mech}). To simplify the calculation of the mechanical resonant frequency of the bondwires, we assume that the wire can be described by a parabolic arc. Then, the resonant frequency of a bondwire can be calculated by [13]

$$\omega_r = C_n \frac{1}{l^2 r}\sqrt{\frac{EI}{\rho}} \tag{2}$$

where I is the second moment of inertia, l is the length of wire, E is the Young's modulus, ρ is the material density, and C_n is a constant for a given vibration mode. Note that C_n is related to l/h, where h is the height of the bondwire arc. For a circular cross section, the second moment of inertia is

$$I = \frac{\pi r^4}{4} \tag{3}$$

where r is the radius of the bondwires. Thus, the mechanical resonant frequency is proportional to the radius but inversely proportional to the length of the bondwire. From (2), the bandwidth of the proposed gold and aluminum bondwire sensor will be limited by the lower resonant frequency of the gold bondwire. Equations (1) and (2) reveal a tradeoff between sensitivity and bandwidth of the sensor. Sensors using longer bondwires have a lower resonant frequency (and thus bandwidth) but will be more sensitive due to larger displacements. These design parameters can be controlled and optimized to match the desired application. Based on these design considerations, a pair of 3.5-mm-long, 1-mil-diameter bondwires were chosen for our sensor. The bondwire spacing is set by the minimum pitch of the

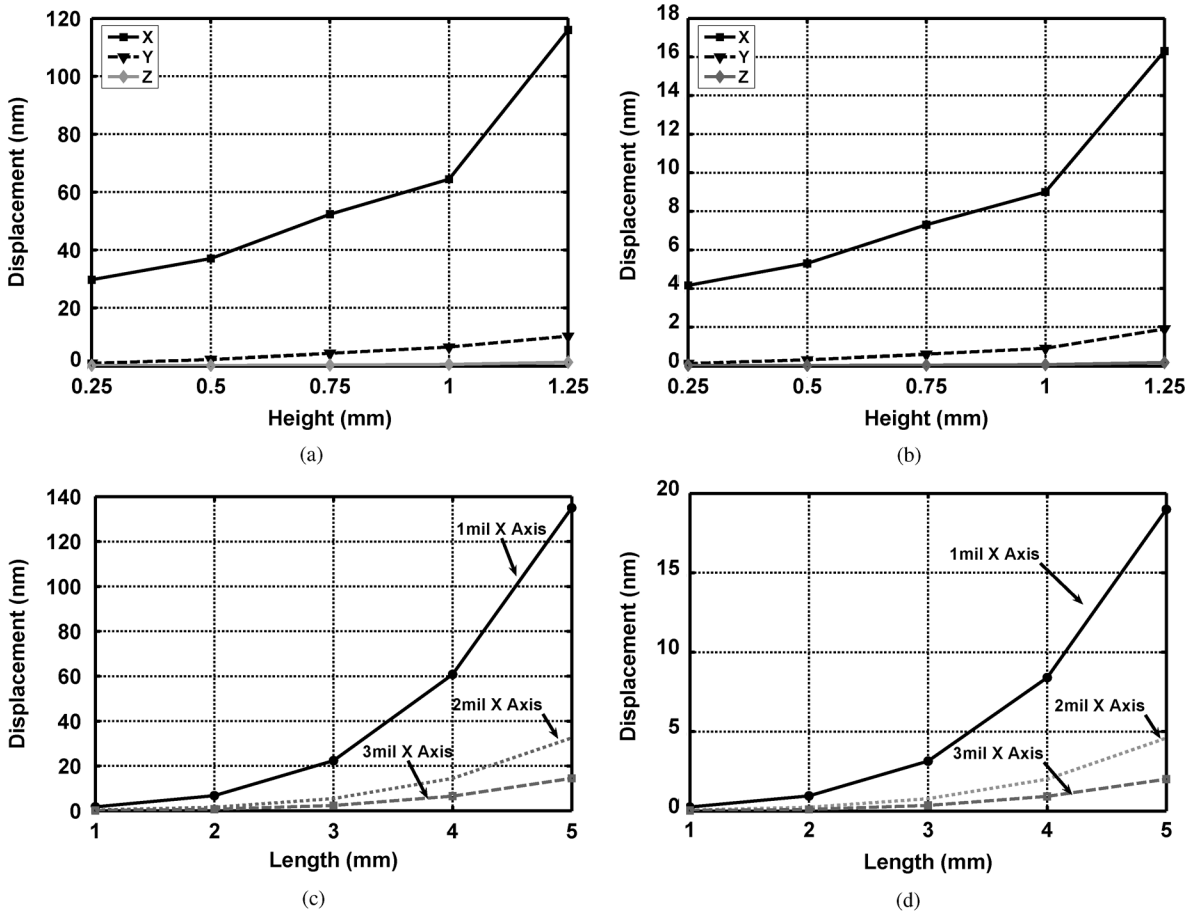

Fig. 3. Simulated bondwire displacement plotted against different arc heights (a) Au and (b) Al (length = 3.5 mm, diameter = 1 mil) and lengths and diameters (c) Au and (d) Al (height = 0.5 mm) at 1-g acceleration.

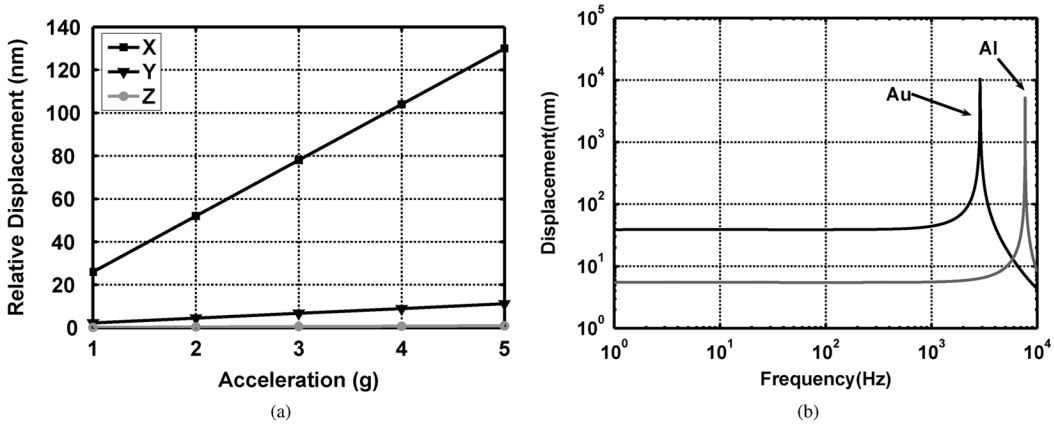

Fig. 4. Simulated (a) gain and (b) frequency response (length = 3.5 mm, diameter = 1 mil, and height = 0.5 mm) for a 1-g acceleration.

bonding pads (90 μm). The mechanical performance was characterized by FEM simulation. Fig. 4(a) shows a linear gain of 32 nm/g in the major axis (X). Fig. 4(b) shows the frequency response for 3.5-mm-long gold and aluminum bondwires with a diameter of 1 mil and a height of 500 μm. The simulated mechanical resonant frequencies are 2.9 and 8.3 kHz for gold and aluminum bondwires, respectively.

C. Bondwire Inductance

Bondwires appear as explicit or parasitic inductors in RFIC design. Bondwires have a larger surface area per unit length compared to planar spiral inductors and are further from the ground plane. This increased distance from the ground plane reduces parasitic capacitance and resistive and substrate losses, resulting in a high Q inductor. The self and mutual inductance of parallel bondwires can be modeled as given by (4) and (5), shown at the bottom of the following page, where d is the diameter, h is the height from the ground plane, S is the distance between two wires, and l is the length of the bondwire [14]. For two wires carrying differential currents, the effective inductance (L_t) is L–M. For bondwires of fixed length, the effective inductance is approximately linear under acceleration due

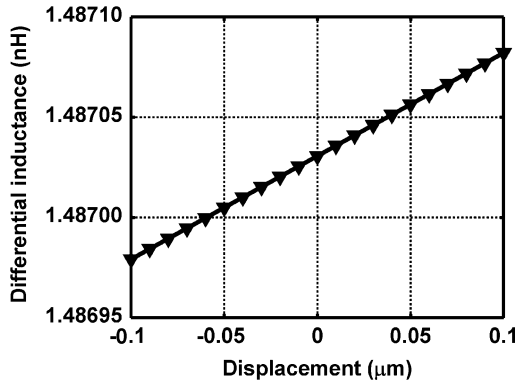

Fig. 5. Simulated differential inductance of bondwires versus displacement (length = 3.5 mm and height = 0.5 mm).

to the proportionality of the mutual inductance to l/S and the small changes in S. The finite-difference time-domain (FDTD) method and quasi-c-static method are used by CAD tools to model bondwire inductance and coupling [15]. Simulated results are shown in Fig. 5. The bondwires are modeled using six-segment coupled transmission lines and show a differential inductance sensitivity of 350 ppm/μm for a pair of 3.5 mm bondwires. Due to the small displacements of the bondwire (and the corresponding small changes in inductance) under acceleration, the oscillator frequency can be linearly approximated as

$$\omega = \frac{1}{\sqrt{C(L_t + \Delta L))}} = \frac{1}{\sqrt{L_t C}}\left(1 - \frac{\Delta L}{2L_t}\cdots\right) \tag{6}$$

where C is an on-chip capacitance that is independent of acceleration. Thus, for a 2-GHz bondwire oscillator with a 30-nm relative displacement due to a 1-g acceleration, we conclude that the center frequency will shift 10.5 kHz, which is detectable by a conventional demodulator. This equation reveals that a 10% variation in inductance will result in a 50-mg gain deviation while the oscillator frequency is fixed. This gain error can be calibrated by on-chip tuning scheme.

IV. Noise Analysis

One of the challenges in this sensor architecture is detecting the small induced frequency deviation which can be overwhelmed by noise. Noise sources in an accelerometer consist of the mechanical noise of the sensor and the noise of the readout electronics. These contributions will be discussed in the following subsections on mechanical and front-end oscillator noise.

A. Mechanical Noise

The mechanical noise of the system can be characterized by the Brownian motion of the structure. Brownian motion, a type of mechanical-thermal noise that is caused by molecular collisions from the surrounding environment, represents the fundamental noise limit of an inertial sensor. The Brownian noise equivalent acceleration (BNEA) can be calculated by [16]

$$\mathrm{BNEA} = \frac{\sqrt{4K_BTD}}{M_a} = \sqrt{\frac{4K_BT\omega_r}{Q_{\mathrm{Mech}}M}} \tag{7}$$

where K_B is Boltzmann's constant, T is absolute temperature, D is the damping coefficient, M_a is the proof mass, ω_r is mechanical self-resonant frequency, and Q_{Mech} is the mechanical quality factor. Microstructures with large mass and high quality factors are needed to reduce the noise from Brownian motion in an accelerometer design. From simulation, a 3.5-mm-long Au bondwire has a $M_a = 30$ μg, $\omega_r = 3$ kHz, and $Q_{\mathrm{Mech}} = 200$, which leads to the input-referred noise density of approximately 0.73 $\mu g/\sqrt{\mathrm{Hz}}$ at room temperature. This value can be further reduced by operating the accelerometer in vacuum, which would eliminate viscus dampling and result in a higher Q_{Mech}.

B. Front-End Oscillator Noise

In addition to the fundamental mechanical noise, minimizing electronic noise is critical. The residual frequency is an important specification which defines the RMS value of the frequency fluctuation within a frequency range. The residual frequency can be derived from the phase noise of an oscillator as

$$\Delta f = \sqrt{2\int_{f_1}^{f_2} \mathcal{L}(f_m) {f_m}^2 df_m} \tag{8}$$

where $\mathcal{L}(f_m)$ is the single sideband (SSB) noise power spectral density and f_m is the offset from the carrier frequency. As a first pass, the phase noise of an oscillator can be modeled by Leeson's phase-noise formula [17]

$$\mathcal{L}(f_m) = \frac{1}{2}\cdot\left(\frac{1}{Q}\frac{f_{\mathrm{osc}}}{f_m}\right)^2 \frac{FK_bT}{P_{rf}} \tag{9}$$

where F is the oscillator noise factor, Q is the quality factor of the resonant tank, T is the absolute temperature, and P_{rf} is the average power at the output of the oscillator. The integration in (8) can be performed by using a known phase-noise profile within the sensor bandwidth. Fig. 6 shows the calculated

$$L = \frac{\mu_0}{2\pi}\cdot l\left[\ln\left(\frac{4h}{d}\right) + \ln\left(\frac{l+\sqrt{l^2+d^2/4}}{l+\sqrt{l^2+4h^2}}\right) + \sqrt{1+\frac{4h^2}{l^2}} - \sqrt{1+\frac{d^2}{4l^2}} - 2\frac{h}{l} + \frac{d}{2l}\right] \tag{4}$$

$$M = \frac{\mu_0}{2\pi}\cdot l\left[\ln\left(\frac{l}{S} + \sqrt{1+\left(\frac{l}{S}\right)^2}\right) + \sqrt{1+\left(\frac{l}{S}\right)^2} - \sqrt{1+\left(\frac{S}{l}\right)^2} + \frac{S}{l}\right] \tag{5}$$

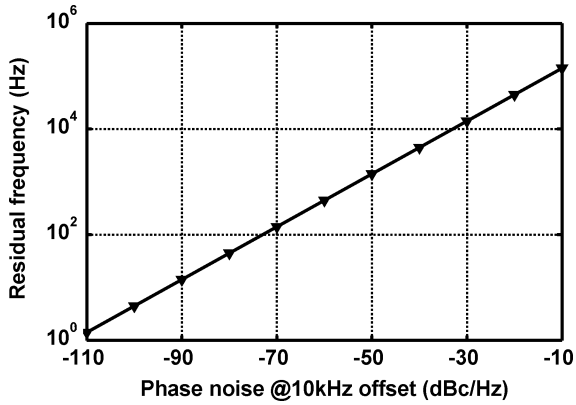

Fig. 6. Calculated residual frequency versus different phase-noise levels at a 10-kHz offset.

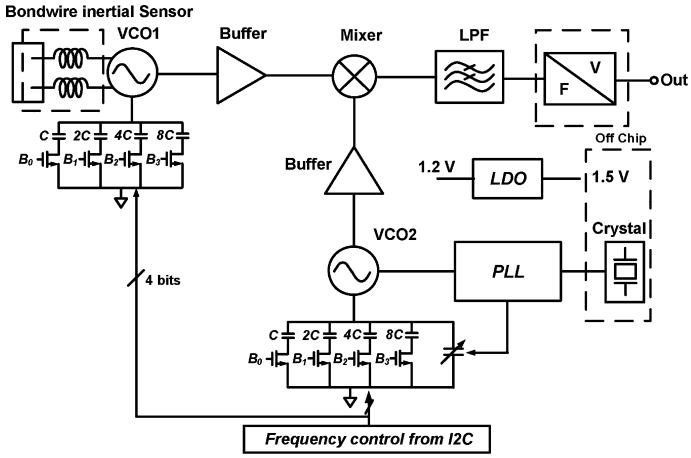

Fig. 7. Top-level schematic of the proposed system.

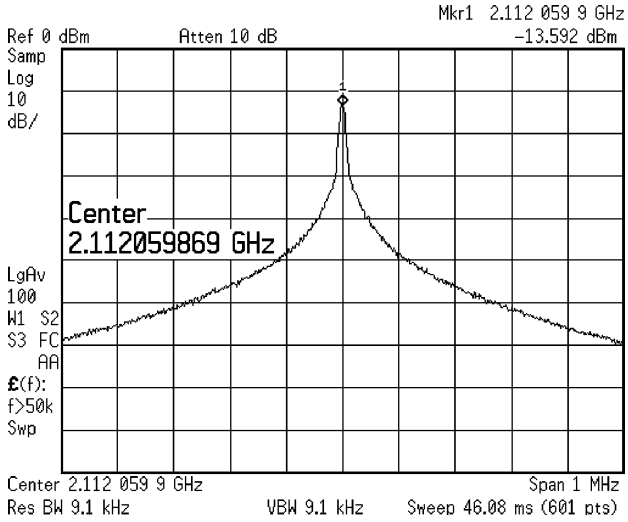

(a)

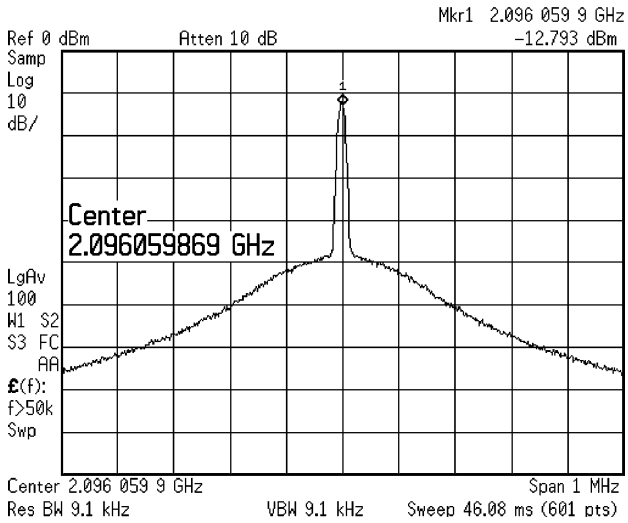

(b)

Fig. 8. Measured spectrum of a (a) free-running and (b) PLL-locked oscillator.

residual frequency for different phase noise levels at 10 kHz with an integration window from 1 Hz to 5 kHz. Assuming the gain of the accelerometer is 10 kHz/g, and assuming a phase-noise slope of −20 dB/decade, the oscillator requires a phase noise of approximately −50 dBc/Hz at a 10 kHz offset to achieve a full bandwidth resolution of 0.1 g. The resolution can be further improved by increasing the power consumption of the oscillator, using a higher Q resonant tank, or limiting the bandwidth of the sensor signal.

V. System and Circuit Implementation

A. System Overview

Fig. 7 illustrates the overall block diagram of the implemented inertial sensor readout system. The interface circuitry relies on a fully differential architecture to mitigate common-mode noise and power supply noise. The sensor readout circuit comprises a 2-GHz sensing oscillator, phase-locked loop (PLL), downconverter, baseband amplifier, and a bandgap-stabilized low-dropout (LDO) supply regulator. VCO1 is the sensing oscillator, which has its oscillation frequency modulated by the deviation in bondwire inductance. A second-order PLL provides a stable quartz-locked frequency reference (VCO2). Fig. 8 shows the measured spectrum of the free-running oscillator and the PLL-locked oscillator. The in-band noise of the locked oscillator is suppressed by the loop. Thus, the noise of the system is dominated by the free-running oscillator (VCO1). The loop bandwidth of the PLL is 50 kHz, setting an upper bound for the applied acceleration frequency. Acceleration above that frequency is not suppressed by the PLL and will result in signal cancellation. In any case, it is outside the bandwidth of our inertial sensor. In addition, the control voltage of the PLL can be used to calibrate the temperature-caused and longterm frequency drifts of the bondwire oscillator. The frequency output from VCO1 is downconverted to 20 MHz for easy detection and to prevent the two oscillators from frequency locking (undesired synchronization). To reduce digital switching noise coupling, the digital and analog supplies use separate regulators.

B. Circuit Block Implementation

Fig. 9 shows the 2-GHz bondwire sensing oscillator. To reduce noise up-conversion due to nonlinearity, varactors were

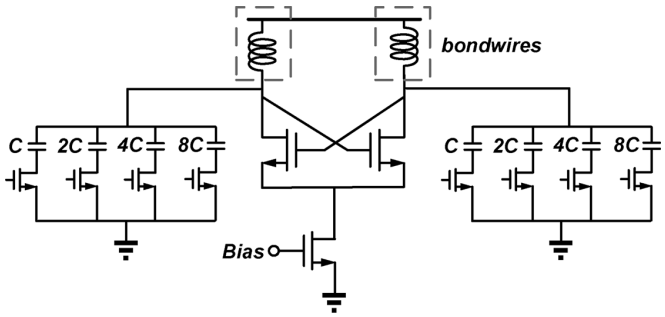

Fig. 9. Schematic of the bondwire oscillator.

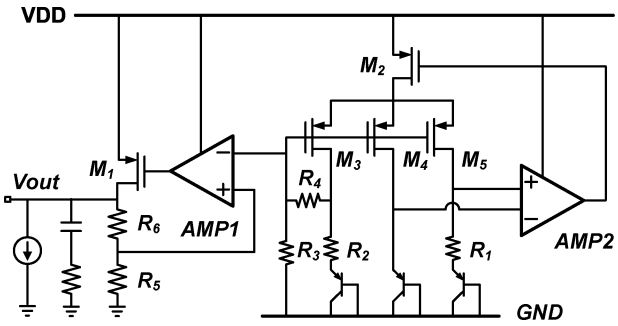

Fig. 10. Schematic of the LDO regulator.

avoided. In order to compensate for variations in the wire-bonding process and fabrication, the oscillator is tunable from 1.5 to 2.5 GHz by utilizing a 4-b discrete capacitor bank. A similar oscillator with a varactor is employed in an integer-N PLL. The frequency deviation between the two oscillators is established by the divide ratio N and programmable in 8-MHz steps. To further enhance the power-supply-rejection-ratio (PSRR) and reduce the temperature dependency of the sensing oscillator's frequency, an on-chip bandgap reference and LDO regulator (LDO) is used to convert a 1.5-V external battery supply to a clean, internal, 1.2-V supply. The LDO is shown in Fig. 10 and consists of a temperature-stabilized bandgap reference and an error amplifier. Combined with a PMOS output stage, this topology can achieve a low-dropout regulation without the need for a large overdrive voltage. A bandgap reference is used to provide a stable biasing voltage over temperature variation. In order to further enhance supply rejection, the bandgap reference is regulated by adding M_2 and controlled by an error amplifier. The bias voltage at the gates of $M_3 - M_5$ is from the output of the bandgap reference, creating a negative feedback loop that enhances stability. The regulator can accommodate a load current up to 16 mA with a 10-mV drop from 1.2 V at the output. Fig. 11 shows the measured voltage output of the regulator versus temperature (0 °C–100 °C) and input voltage (1.3–1.6 V). The maximum voltage deviation is 7 mV across temperature and the measured low-frequency PSRR is 32 dB from 1.35 to 1.55 V.

The RF mixer downconverts the modulated RF signal to a low frequency to facilitate demodulation. Unlike conventional FM receivers, the mixer in this design is driven by two large signals. Though this provides noise immunity, it also leads to signal distortion and LO pulling that can overwhelm the input signal.

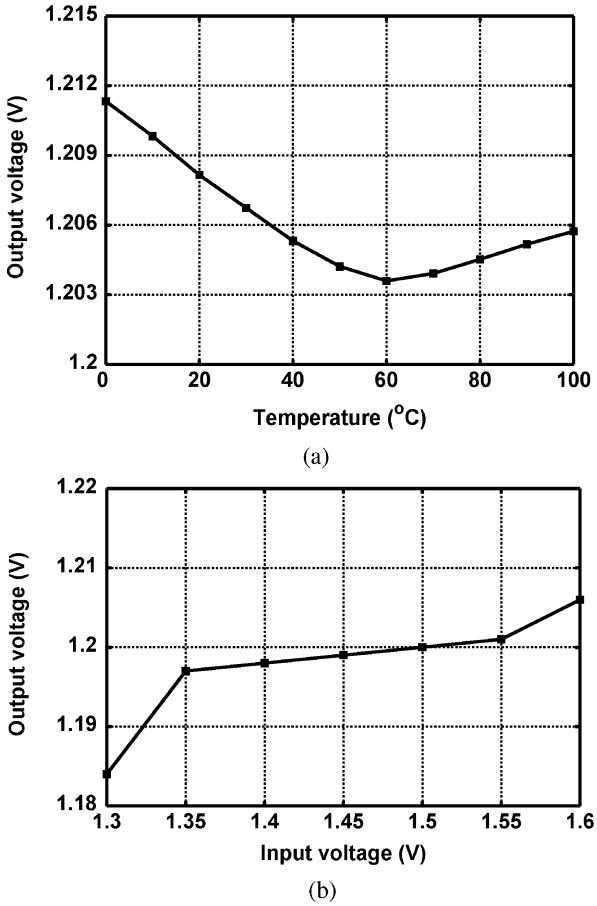

Fig. 11. Measured regulator output voltage over (a) temperature and (b) voltage.

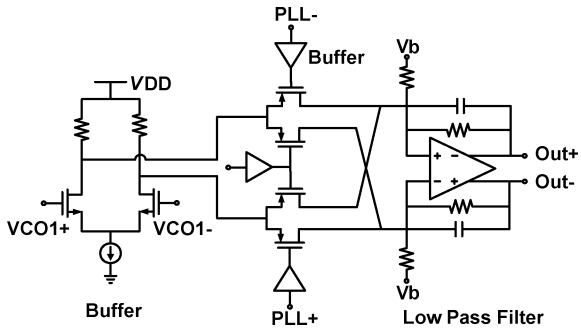

Fig. 12. Schematic of the double-balanced mixer.

CMOS passive mixers have been demonstrated to produce better linearity and low flicker noise [18]. A two-stage cascaded buffer inserted between the oscillator and the mixer reduces the effect of the local oscillator (LO) pulling in the sensing oscillator. The double balanced topology, as shown in Fig. 12, cancels the LO feedthrough and offsets at the output. The third order active *RC* low-pass filter amplifies the signals and consequently reduces the effect of amplitude induced errors in the baseband demodulator.

VI. Experimental Results

Fig. 13 shows the micrograph of the prototype accelerometer fabricated in a 0.13-μm CMOS process. The accelerometer

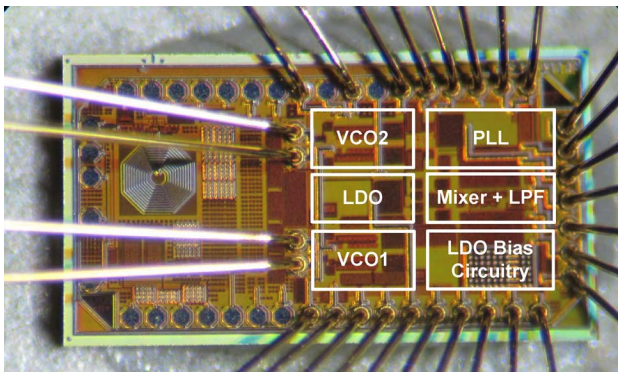

Fig. 13. Micrograph of the accelerometer IC. The active area is outlined in white (online version) boxes.

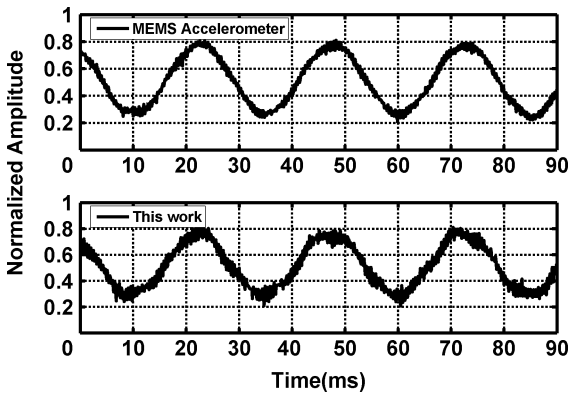

Fig. 14. Measured waveforms of the bondwire and commercial accelerometer under 1-g acceleration at 40 Hz.

is completely integrated except for an 8-MHz quartz crystal and bypass capacitors. The chip was mounted in a 44-pin plastic leaded chip carrier (PLCC) using aluminum/gold wedge wire bonding without encapsulation and powered by one AA battery. The stiffness of the PLCC isolates the bondwires from frequency shifts induced by PCB strain or other undesired external forces. Two commercial accelerometers were mounted on the PCB near the chip to ensure accurate calibration of the applied acceleration from a shaker table. The prototype PCB was mounted on a custom machined aluminum platform to maximize the mechanical energy transferred from the shaker to the accelerometers. The outputs were monitored by an oscilloscope and a spectrum analyzer. The waveforms at the output of the bondwire accelerometer and a commercial MEMS accelerometer are shown in Fig. 14. We applied an acceleration of 1 g at 40 Hz along the sensitive axis (X) and normalized the output amplitude to the gain of the different accelerometers. Fig. 15 shows the measurement results of a three-axis acceleration test on the bondwire accelerometer, revealing a linear gain of 10 kHz/g (matching calculations) and greater than 20-dB isolation between the sensitive axis (X) and nonsensitive axes (Y and Z). As a control, the same test was performed on a chip which was completely encapsulated in nonconductive epoxy (*Stycast 1266*). The goal of this experiment was to decisively show that the frequency deviations under acceleration were caused by bondwire deflection. The control package exhibited no detectable output from acceleration along any axis. A 90° rotation test with acceleration only from gravity was performed,

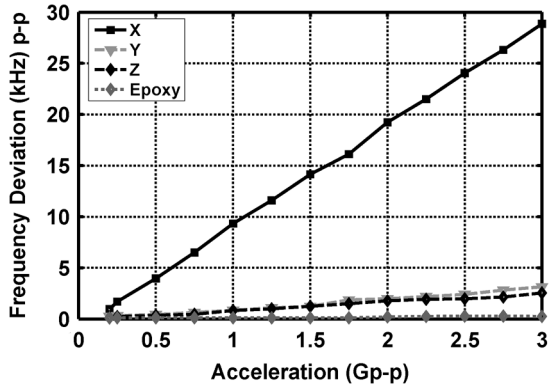

Fig. 15. Measurement results of a three-axis acceleration test.

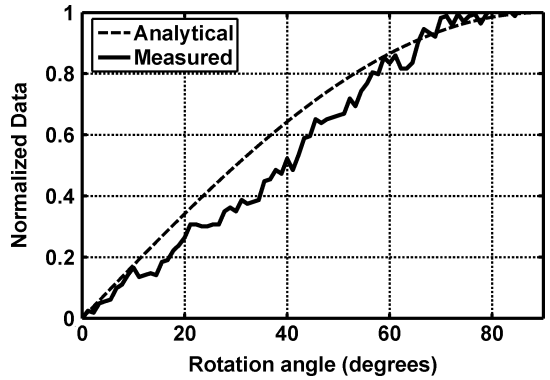

Fig. 16. Measurement results of a rotation test.

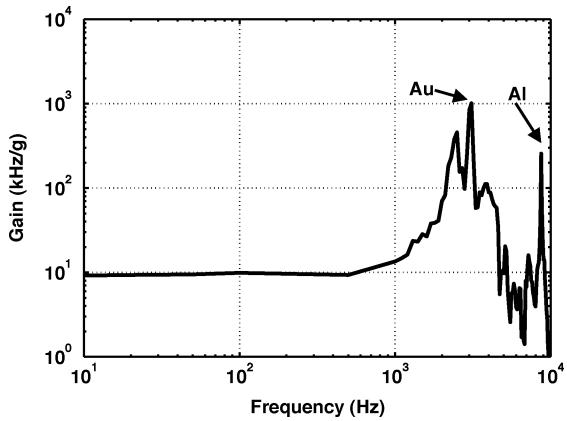

Fig. 17. Measured frequency response of the bondwire accelerometer.

and the result is plotted alongside the expected sinusoidal response in Fig. 16. Fig. 17 shows the measured accelerometer frequency response, exhibiting a gain of 10 kHz/g within a 700-Hz bandwidth. The mechanical resonances of the Au and Al bondwires are visible at approximately 3.1 and 8.7 kHz, respectively, which is consistent with the FEM simulation.

The bondwires exhibit a high electrical quality factor ($Q{\sim}40$), allowing a low sensor oscillator phase noise of -64 dBc/Hz and -121 dBc/Hz at 10-kHz and 1-MHz offsets, respectively, while consuming 2 mA. Fig. 18(a) shows the measured phase noise of the sensing oscillator, PLL, and IF stage, confirming that the accelerometer noise floor is dominated by the free-running sensor oscillator. The Allan variance is often used to define a clock system and sensor performance [19]. Fig. 18(b) shows the measured Allan variance of the outputs of

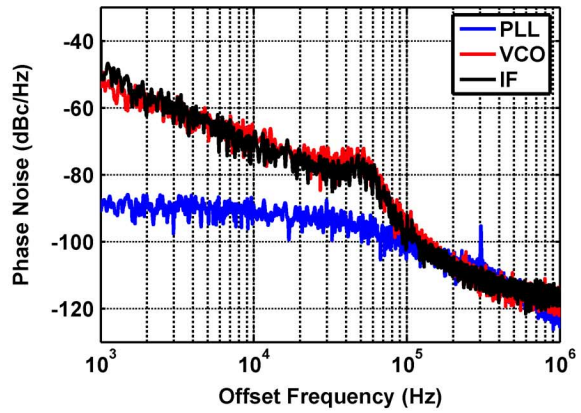

(a)

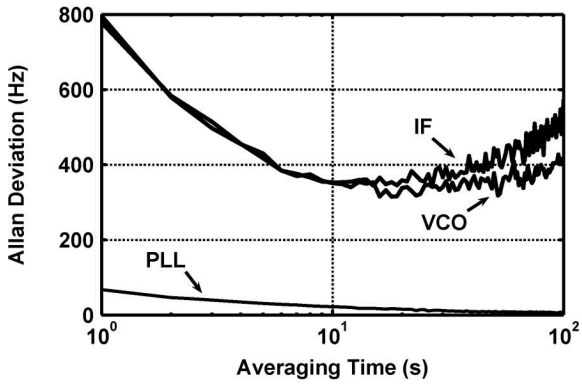

(b)

Fig. 18. Measured (a) phase noise and (b) Allan variance at the outputs of the sensing oscillator, PLL, and IF stage.

TABLE II
PERFORMANCE SUMMARY

Technology	0.13μm CMOS
Chip Area	1x1.1mm^2
Oscillator Freq	2.1GHz
PN@10KHz PN@1MHz	-64dBc/Hz -121dBc/Hz
Sensitivity	10kHz/g
Bandwidth	700Hz
Axis isolation	>20dB
Resolution	80mg
Bias stability	35mg
Power consumption	13.5mW

the sensing oscillator, PLL, and IF with a sample rate of 1 Hz. The Allan variance gradually flattens out as the average time increases. The drift is believed to be caused by the temperature and environment fluctuation that can be removed by a feedback control to VCO1. The measured temperature coefficient of VCO1 is 165 ppm/°C (0–100°C). Further, this plot reveals that the accelerometer has a resolution of 80 mg and a bias stability of 35 mg for a 10 second integration window. The noise floor of this accelerometer is limited by the phase noise of the sensing oscillator, not by mechanical noise sources. The accelerometer performance is summarized in Table II.

In a batch of sensors, a Gaussian distribution of height and mean separation exists in the Al and Au bondwires due to random bondwire process variation. Both L_t and ΔL in (6) are affected. The variation in L_t is an offset error in ω, which was measured to be up to 10%, and can be calibrated by using a 4-b on-chip capacitor array. The variation in ΔL affects the sensitivity of the sensor and is approximately proportional to the variation in bondwire separation. The largest contribution of variance in bondwire separation comes from bonding off-chip. This source of error can be mitigated by bonding precisely between two on-chip pads.

VII. CONCLUSION

We presented a low-cost implementation of an inertial sensor using two adjacent bondwires with differing material properties. The peak 1-g displacements of 3.5-mm-long and 0.5-mm-high gold and aluminum wires were simulated to be 37 and 5.3 nm respectively, which gives an inductive change of 350 (ppm/μm). A bondwire accelerometer was fabricated with a chip area of 1.1 mm^2 in a standard 0.13-μm CMOS process without post processing. A bandwidth of 700 Hz and a sensitivity of 10 kHz/gf were measured with a power consumption of 13.5 mW. The accelerometer was used to demonstrate orientation and tilt applications with a resolution of 80 mg. These measurement results were supported by theoretical calculations and FEM simulation results. In the future, temperature stabilization, digital data processing/calibration, and wireless data transmission can be employed with this prototype accelerometer on the same silicon substrate.

ACKNOWLEDGMENT

The authors would like to thank Dr. R. Baskaran, S. Zafonte, D. Yeager, A. Lingley, and B. Chen for their assistance.

REFERENCES

[1] N. Barbour and G. Schmidt, "Inertial sensor technology trends," *IEEE Sensors J.*, vol. 1, no. 4, pp. 332–339, Dec. 2001.
[2] N. Yazdi, F. Ayazi, and K. Najafi, "Micromachined inertial sensors," *Proc. IEEE*, vol. 86, no. 8, pp. 1640–1659, Aug. 1998.
[3] M. Paavola, M. Kamarainen, J. Jarvinen, M. Saukoski, M. Laiho, and K. Halonen, "A micropower interface ASIC for a capacitive 3 axis micro-accelerometer," *IEEE J. Solid-State Circuits*, vol. 42, no. 12, pp. 2651–2665, Dec. 2007.
[4] C. Hindrichsen, N. Almind, S. Brodersen, O. Hansen, and E. Thomsen, "Analytical model of a PZT thick-film triaxial accelerometer for optimum design," *IEEE Sensors J.*, vol. 9, no. 4, pp. 419–429, Apr. 2009.
[5] B. Bhola and W. Steier, "A novel optical microring resonator accelerometer," *IEEE Sensors J.*, vol. 7, no. 12, pp. 1759–1766, Dec. 2007.
[6] G. H. Ames and J. M. Maguire, "Erbium fiber laser accelerometer," *IEEE Sensors J.*, vol. 7, no. 4, pp. 557–561, Apr. 2007.
[7] C.-H. Liu and T. Kenny, "A high-precision, wide-bandwidth micromachined tunneling accelerometer," *J. Microelectromech. Syst.*, vol. 10, no. 3, pp. 425–433, Sep. 2001.
[8] H. Takao, H. Fukumoto, and M. Ishida, "A CMOS integrated three axis accelerometer fabricated with commercial submicrometer CMOS technology and bulk-micromachining," *IEEE Trans. Electron Devices*, vol. 48, no. 9, pp. 1961–1968, Sep. 2001.
[9] B. Amini, R. Abdolvand, and F. Ayazi, "A 4.5-mW closed-loop $\Delta\Sigma$ micro-gravity CMOS SOI accelerometer," *IEEE J. Solid-State Circuits*, vol. 41, no. 12, pp. 2983–2991, Dec. 2006.
[10] M. Lemkin and B. Boser, "A three axis micromachined accelerometer with a CMOS position-sense interface and digital offset-trim electronics," *IEEE J. Solid-State Circuits*, vol. 34, no. 4, pp. 456–468, Apr. 1999.
[11] Y.-T. Liao, W. Biederman, and B. Otis, "A CMOS accelerometer using bondwire inertial sensing," in *Proc. Symp. VLSI Circuits*, Jun. 2009, pp. 64–65.
[12] T. Marinis and J. Soucy, "Design and characterization of wirebonds for use in high shock environments," in *Proc. 59th Electron. Compon. Technol. Conf.*, May 2009, pp. 1414–1422.

[13] H. A. Schafft, "Testing and fabrication of wire-bond electrical connections: A comprehensive survey," Nat. Bureau of Standards Tech., Note 726, Sep. 1972.
[14] I. J. Bahl, *Lumped Elements for RF and Microwave Circuits*. Norwood, MA: Artech House, 2003.
[15] F. Alimenti, P. Mezzanotte, L. Roselli, and R. Sorrentino, "Modeling and characterization of the bonding-wire interconnection," *IEEE Trans. Microw. Theory Tech.*, vol. 49, no. 1, pp. 142–150, Jan. 2001.
[16] B. Boser and R. Howe, "Surface micromachined accelerometers," *IEEE J. Solid- State Circuits*, vol. 31, no. 3, pp. 366–375, Mar. 1996.
[17] D. Leeson, "A simple model of feedback oscillator noise spectrum," *Proc. IEEE*, vol. 54, no. 2, pp. 329–330, Feb. 1966.
[18] S. Zhou and M.-C. Chang, "A CMOS passive mixer with low flicker noise for low-power direct-conversion receiver," *IEEE J. Solid-State Circuits*, vol. 40, no. 5, pp. 1084–1093, May 2005.
[19] N. El-Sheimy, H. Hou, and X. Niu, "Analysis and modeling of inertial sensors using allan variance," *IEEE Trans. Instrum. Meas.*, vol. 57, no. 1, pp. 140–149, Jan. 2008.

Yu-Te Liao (S'05) received the B.S. degree in electrical engineering from National Cheng Kung University, Tainan, Taiwan, in 2003, the M.S. degree in electronics engineering from National Taiwan University, Taipei, Taiwan, in 2005, and is currently working toward the Ph.D. degree at the University of Washington, Seattle.

His research interests include low-power RF integrated circuits, integrated sensors, and biomedical circuits and systems.

William J. Biederman (S'07) received the B.S. degree (*magna cum laude*) in electrical engineering from the University of Washington, Seattle, in 2009, and is currently working toward the Ph.D. degree in electrical engineering at the University of California, Berkeley.

During 2007, he was with NASA's Jet Propulsion Laboratory (JPL), developing methods of wireless power transmission. He authored or coauthored several papers about his work at JPL. His research interests include wireless sensing and energy scavenging.

Mr. Biederman was the recipient of the National Defense Science and Engineering Graduate Fellowship in 2009 and the National Science Foundation Graduate Research Fellowship in 2010.

Brian P. Otis (S'96–M'05–SM'10) received the B.S. degree from the University of Washington, Seattle, and the M.S. and Ph.D. degrees from the University of California, Berkeley (UC Berkeley), all in electrical engineering.

He joined the faculty of the University of Washington as an Assistant Professor of electrical engineering in 2005. His primary research interests are ultralow-power RF integrated-circuit design and bioelectrical interface circuits and systems. He previously held positions at Intel Corporation and Agilent Technologies.

Dr. Otis was an Associate Editor of the IEEE TRANSACTIONS ON CIRCUITS AND SYSTEMS II: EXPRESS BRIEFS. He was the recipient of the National Science Foundation CAREER Award in 2009 and the UC Berkeley Seven Rosen Funds Award for Innovation in 2003 and was corecipient of the 2002 ISSCC Jack Raper Award for an Outstanding Technology Directions Paper.